

Time-resolved resting-state brain networks

Andrew Zalesky^{a,b,1}, Alex Fornito^{a,c}, Luca Cocchi^d, Leonardo L. Gollo^e, and Michael Breakspear^{e,f,g}

^aMelbourne Neuropsychiatry Centre, The University of Melbourne and Melbourne Health, Melbourne, VIC 3010, Australia; ^bMelbourne School of Engineering, The University of Melbourne, Melbourne, VIC 3010, Australia; ^cMonash Clinical and Imaging Neuroscience, School of Psychological Sciences and Monash Biomedical Imaging, Monash University, Melbourne, VIC 3168, Australia; ^dQueensland Brain Institute, The University of Queensland, Brisbane, QLD 4072, Australia; and ^eQIMR Berghofer Medical Research Institute, ^fThe Royal Brisbane and Women's Hospital, and ^gMetro North Mental Health, Brisbane, QLD 4029, Australia

Edited by Michael S. Gazzaniga, University of California, Santa Barbara, CA, and approved May 19, 2014 (received for review January 13, 2014)

Neuronal dynamics display a complex spatiotemporal structure involving the precise, context-dependent coordination of activation patterns across a large number of spatially distributed regions. Functional magnetic resonance imaging (fMRI) has played a central role in demonstrating the nontrivial spatial and topological structure of these interactions, but thus far has been limited in its capacity to study their temporal evolution. Here, using high-resolution resting-state fMRI data obtained from the Human Connectome Project, we mapped time-resolved functional connectivity across the entire brain at a subsecond resolution with the aim of understanding how nonstationary fluctuations in pairwise interactions between regions relate to large-scale topological properties of the human brain. We report evidence for a consistent set of functional connections that show pronounced fluctuations in their strength over time. The most dynamic connections are intermodular, linking elements from topologically separable subsystems, and localize to known hubs of default mode and frontoparietal systems. We found that spatially distributed regions spontaneously increased, for brief intervals, the efficiency with which they can transfer information, producing temporary, globally efficient network states. Our findings suggest that brain dynamics give rise to variations in complex network properties over time, possibly achieving a balance between efficient information-processing and metabolic expenditure.

network efficiency | dynamic connectivity | time-dependent network

The coordination of brain activity between disparate neural populations is a dynamic and context-dependent process (1–3). Although dynamic patterns of neural synchronization may be evident in time-dependent measures of functional connectivity (4, 5), the temporal stability of high-level topological properties is unknown. The topology of large-scale cortical activity—such as its efficient network layout (6), community structure (7), network hubs (8), rich-club organization (9, 10), and small worldness (11, 12)—may reflect fundamental aspects of cortical computation. Temporal fluctuations in these graph-theoretic measures may hence speak to adaptive properties of neuronal information processing.

With international connectome mapping consortia such as the Human Connectome Project (HCP) (13) and the developing Human Connectome Project in full swing, resting-state functional magnetic resonance imaging (rsfMRI) data of unprecedented temporal resolution are now available to map the time-resolved properties of functional brain networks. Imaging the brain at rest reveals spontaneous low-frequency fluctuations in brain activity that are temporally correlated between functionally related regions (14–17). Interregional correlations are referred to as functional connections, and they collectively form a complex network (18).

Functional brain networks are typically mapped in a time-averaged sense, based on the assumption that functional connections remain relatively static (stationary) in the resting brain. However, recent investigations have furnished compelling evidence challenging the “static” conceptualization of resting-state functional connectivity (5). In particular, the application of time-resolved methodologies for analyzing time series data has

consistently revealed fluctuations in resting-state functional connectivity at timescales ranging from tens of seconds to a few minutes (19–24). Furthermore, the modular organization of functional brain networks appears to be time-dependent in the resting state (25, 26) and modulated by learning (27) and cognitive effort (28, 29). It is therefore apparent that reducing fluctuations in functional connectivity to time averages has led to a very useful but static and possibly oversimplified characterization of the brain’s functional networks. For example, connections that toggle between correlated and anticorrelated states are reduced to zero in a time-averaged sense, assuming equal dwell times in each state.

Conventionally, rsfMRI data are sampled at a resolution of 2 s or slower. Using multiband accelerated echo planar imaging, the HCP has acquired high-quality rsfMRI data at a subsecond resolution (30). This order of magnitude improvement in temporal resolution is highly advantageous to the feasibility of time-resolved functional connectomics. Faster sampling rates enable a richer temporal characterization of resting-state fluctuations, denser sampling of physiological confounds, and greater degrees of freedom (30).

Using a sliding-window approach applied to HCP rsfMRI data, we mapped the evolution of functional brain networks over a continuous 15-min interval at a subsecond resolution. For each of 10 individuals, this yielded a time series of correlation matrices (regions × regions × time), where matrix elements quantified the functional connectivity at a given time instant between cortical and subcortical regions comprising established brain parcellation atlases. We developed a statistic to test the time-resolved connectome for evidence of nonstationary temporal dynamics and applied it to the 10 individuals as well as a replication data set and simulated rsfMRI data.

Our main aim was to investigate the consequences of nonstationary fluctuations on the topological organization of

Significance

Large-scale organizational properties of brain networks mapped with functional magnetic resonance imaging have been studied in a time-averaged sense. This is an oversimplification. We demonstrate that brain activity between multiple pairs of spatially distributed regions spontaneously fluctuates in and out of correlation over time in a globally coordinated manner, giving rise to sporadic intervals during which information can be efficiently exchanged between neuronal populations. We argue that dynamic fluctuations in the brain’s organizational properties may minimize metabolic requirements while maintaining the brain in a responsive state.

Author contributions: A.Z., A.F., L.C., L.L.G., and M.B. designed research; A.Z., A.F., L.C., L.L.G., and M.B. performed research; A.Z. contributed new reagents/analytic tools; A.Z., A.F., L.C., L.L.G., and M.B. analyzed data; and A.Z., A.F., L.C., L.L.G., and M.B. wrote the paper.

The authors declare no conflict of interest.

This article is a PNAS Direct Submission.

Freely available online through the PNAS open access option.

¹To whom correspondence should be addressed. E-mail: azalesky@unimelb.edu.au.

This article contains supporting information online at www.pnas.org/lookup/suppl/doi:10.1073/pnas.1400181111/-DCSupplemental.

functional brain networks. We hypothesized that dynamic behavior is coordinated across the brain so that transitions between distinct states are marked by reorganization of the brain's functional topology. Evidence for this hypothesis is provided by the coordinated fluctuations in network measures, such as hub centrality (31), that have been observed in simulated rsfMRI data (32, 33).

Results

Time-resolved functional brain connectivity was mapped using a sliding-window approach applied to high-resolution rsfMRI data acquired in 10 healthy, young adults participating in the HCP (*Materials and Methods*). Connectivity was estimated using pairwise linear correlation in regionally averaged rsfMRI time series data falling within fixed-length time windows (19, 21, 22, 26). We used a tapered window of length 60 s (83 time points per window). Sliding the window in time yielded a continuous series of snapshots characterizing the evolution of each individual's functional brain network at a temporal resolution of 720 ms over a 15-min interval.

We developed a statistic to test for time-varying (nonstationary) connectivity. To estimate the statistic's distribution under the null hypothesis of stationarity, 250 null data sets were generated using stable vector autoregressive (VAR) models (34) that approximately preserved the power and cross-spectrum of the actual rsfMRI data (*Materials and Methods* and *SI Appendix*, Fig. S1). The null hypothesis was rejected pairwise when the time-resolved correlation coefficients fluctuated on a timescale longer than the window length and/or between more extreme correlation levels than expected by chance [$P < 0.01$, familywise error rate (FWER) corrected across all connections]. This enabled partitioning of each individual's functional brain network into dynamic (nonstationary) and static (stationary) connections.

We first tested all 6,670 connections defined by the 116-region Automated Anatomical Labeling (AAL) (35) atlas for evidence of time-varying connectivity. Across the 10 individuals, the number of connections for which the null hypothesis of stationarity was rejected varied between 118 and 570 [mean: 293 (~4%); SE: 54]. The top-100 most dynamic connections for each individual, according to test statistic magnitude, could therefore be declared nonstationary for *all* individuals.

An index of consistency was then used to establish whether the top-100 most dynamic connections were consistent (i.e., overlapped) across the 10 individuals. For each individual, a binary graph comprising only the top-100 most dynamic connections was constructed. The degree of each region in these 100-edge graphs was determined and then summed across the 10 individuals to give a region-specific index of consistency/overlap. Regionally sorted from lowest-to-highest overlap, this index of consistency is shown in Fig. 1A for the actual data (blue line) and for the 250 VAR null data sets described above (black lines). The 19 regions residing to the right of the $P = 0.01$ cutoff (vertical red line) were therefore associated with dynamic behavior more consistently than what would be expected by chance alone. Cortical renderings of consistency are shown in Fig. 1B. The 19 regions are as follows: angular gyrus (l/r); supramarginal gyrus (l/r); rectus gyrus (l/r); medial orbitofrontal cortex (l/r); inferior parietal lobule (l/r); inferior frontal operculum (l/r); middle frontal gyrus (l/r); amygdala (r); superior temporal pole (r); olfactory cortex (l); and postcentral gyrus (l) and precentral gyrus (l) with left (l), right (r), and both (l/r) hemispheres. Several of these regions are frontal and parietal association areas that are known hubs of the structural human connectome (36), comprise some parietal areas of the default mode network (37), and include rich-club nodes (9, 10). The cerebellum, vermis, and temporal regions were consistently the least dynamic.

Time-resolved correlation coefficients for the top-100 most dynamic connections are shown in Fig. 2A for two representative individuals and a VAR null data set. It can be seen that fluctuations in the time-resolved correlation coefficients are synchronized across the brain, occurring at distinct moments in time,

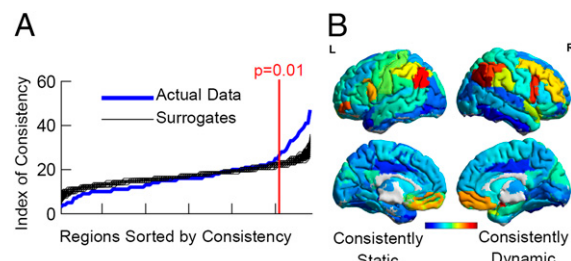


Fig. 1. Regions most consistently forming dynamic functional connections in the resting state. (A) Index of consistency for the actual data (blue line) and 250 null data sets (black lines). The 19 regions residing to the right of the $P = 0.01$ cutoff value (vertical red line) were consistently associated with dynamic behavior across 10 healthy, young adults. (B) Index of consistency rendered onto the cortical surface.

where multiple connections transition en masse between different correlation levels. This is in contrast to the simplest null hypothesis where transitions between correlation levels occur independently among connections.

To test this null hypothesis, the total number of connections (from the top-100 most dynamic connections) that transitioned at each time point was enumerated. This yielded a time series of counts for each individual ranging between 0 and 100, which we referred to as the "transition count." A connection underwent a "transition" at times when its series of time-resolved correlation coefficients crossed their median value. The median correlation value was used here to represent the crossing point between two correlation levels. Using this simple two-state characterization, we tested the null hypothesis of uniformly distributed transitions across time. Null data sets were generated by randomly redistributing groups of related transition events in time, thus preserving synchrony owing to inherent properties of correlation networks (38), but randomizing synchrony resulting from specific aspects of dynamic connectivity (*SI Appendix*). The null hypothesis was rejected within each individual because at least one time point was always found where the transition count exceeded the minimum cutoff, satisfying a FWER of 0.01. Transition counts (blue lines) and the 0.01 FWER cutoff value (horizontal red lines) are provided in Fig. 2B for the same two individuals. The null hypothesis can be rejected at time points where the transition count exceeds the cutoff value. This result verifies that nonstationary fluctuations are synchronized across functional brain networks in such a way that multiple connections transition en masse at distinct moments in time between different correlation levels. Finally, we tested for power law scaling in the distribution of transition counts to establish a possible correspondence with the neuronal avalanche phenomenon (39). However, exponentials and stretched exponentials (40) provided better fits than a power law.

The results displayed in Figs. 1 and 2 were replicated using two different parcellation atlases: Craddock-200 (41) and random-90 (42). Random-90 comprises parcels that are equal in volume. The null hypothesis of uniformly distributed transitions was also rejected when using the top-500 or top-1,000 most dynamic connections.

To further verify this effect, a principal component analysis was performed on the top-100 most dynamic connections to identify any prevailing temporal patterns. For each individual, at least one principal component explaining at least 20% of the variance was present. In comparison, the probability of a principal component explaining at least 20% of the variance in the VAR null data was not significant for all individuals ($P < 0.01$).

Dynamics of Efficiency. We next performed a time-resolved analysis of network efficiency to test whether the dynamic fluctuations that we identified at the pairwise level extend to a complex network property.

A

HCP 105115

HCP 118932

Sample Null Data

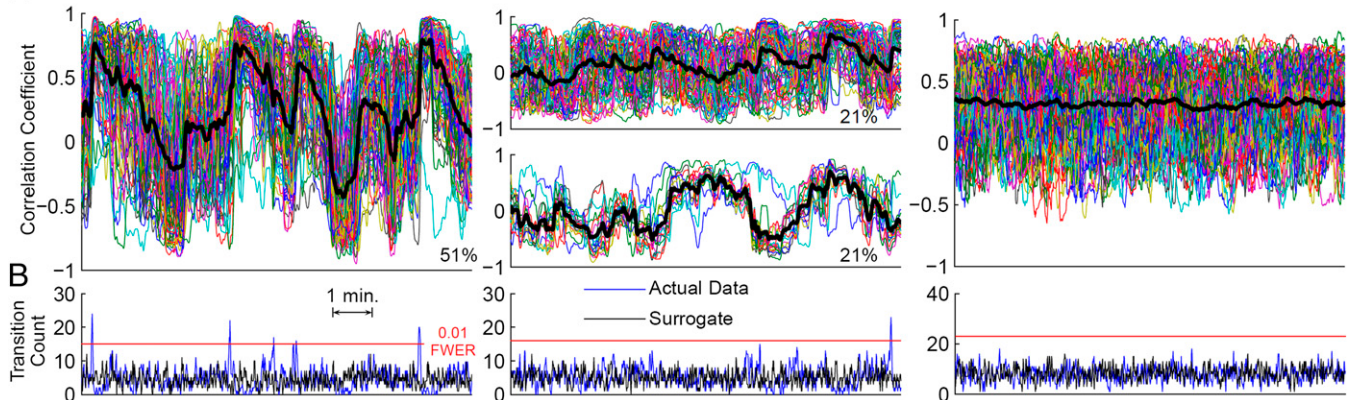


Fig. 2. Dynamic fluctuations are synchronized across resting-state functional brain networks, occurring at distinct moments in time, where multiple connections transition en masse between high and low levels of connectivity. (*A*) Time series of correlation coefficients pertaining to the top-100 most dynamic functional connections for two healthy, young adults and a sample null data set. Percentages indicate the amount of variance explained by the first principal components (thick black lines) accounting for at least 20% of the variance. (*B*) The transition count (blue lines) enumerates for each time point the number of connections that cross their median correlation value. The transition count for a sample null data set is also shown (black lines). The null hypothesis of uniformly distributed transitions across time was rejected at time points when the 0.01 FWER cutoff value (horizontal red lines) was exceeded. Individuals are labeled according to six-digit HCP subject identifiers.

Time-resolved connectivity estimates were thresholded to yield a continuous series of weighted networks, each with a fixed connection density of 20%. Regional efficiencies (43) were calculated for these weighted networks, resulting in a time series of efficiency values for each region (*SI Appendix*). These time-resolved regional efficiencies are shown in Fig. 3*A* for two representative individuals and a VAR null data set. It can be observed that several regions show globally coordinated transitions between low- and high-efficiency states, whereas others show less pronounced fluctuations. No such patterns were observed in the null data. To quantify this observation, the variance in regional efficiency over time was computed in the actual data and in the VAR null data. It was found that the largest variance in efficiency across all 250 null data sets never exceeded the smallest variance in the actual data (*SI Appendix*, Fig. S2), confirming that all regions displayed fluctuations in efficiency that were more variable than the stationary null data. This effect was replicated using several alternative connection densities (*SI Appendix*, Fig. S3) and also observed at the level of global efficiencies (*SI Appendix*, Fig. S4). It can also be observed that transitions from low-to-high efficiencies are sudden, whereas high-to-low transitions are gradual. To quantify this observation, the skewness in the forward difference of time-resolved efficiency was computed in the actual data and in the VAR null data. Forward differences were significantly positively skewed for all individuals ($P < 0.01$; skewness range: 0.17–1.3; *SI Appendix*, Fig. S5).

Cortical renderings of time-resolved regional efficiencies were compiled into movies for two of the individuals featured in Fig. 3*A* (*Movies S1* and *S2* and *SI Appendix*). Snapshots from these movies are shown in Fig. 3*B* at time points residing within an interval spanning a low-efficiency state and at another soon after the transition to a high-efficiency state.

We next tested whether high-efficiency states were more “costly” in terms of the anatomical distance between interconnected regions. Interregional distances were computed for pairs of suprathreshold connections, with the distance between pairs of regions approximated by the Euclidean distance between regional centers of mass. Mean connection length in high-efficiency states was then estimated by averaging these interregional distances over all time points where the global efficiency value exceeded its median. This was repeated for all individuals to yield an estimate of the mean connection length in low- and high-efficiency states. When pooling data across the original and replication data sets (see below), connections were found to be

significantly longer in the high-efficiency states ($P < 0.01$; low: 67.1 ± 2.1 mm; high: 73 ± 1.9 mm).

Network efficiency is thought to reflect a network’s capacity for information transfer (6). High-efficiency networks may be energy demanding (43, 44), as suggested by increased cerebral blood flow to the strong, long-range functional connections facilitating integration across disparate network elements (45). Sporadic emergence of metabolically costly, high-efficiency states lasting for brief intervals may have evolved to minimize energy demands while maintaining the connectome in a globally integrated, responsive state.

Dynamics of Modular Organization. Modules refer to communities of regions that are more strongly interconnected with each other than with regions outside their community. Time-resolved modularity analysis (46) suggests that modular organization of functional brain networks is dynamic (25) and shaped by learning-dependent plasticity (27). We performed a conventional, time-averaged modular decomposition of functional brain networks (7) to understand the spatiotemporal dynamics of inter- and intramodular connections.

An algorithm to determine a modular decomposition representing consensus among the 10 individuals yielded four modules (*SI Appendix*). Modules rendered onto the cortical surface are shown in Fig. 4*A* and broadly overlap established resting-state networks, although the correspondence is not precise because modules were constrained to conform to coarse AAL regional boundaries. The values of the statistic used to test whether a connection was static/dynamic are shown in Fig. 4*B* in matrix form and averaged across the 10 individuals. The four blocks positioned along the matrix diagonal correspond to modules and encapsulate intramodular connections. The visual, default mode and somatomotor modules can be seen to comprise disproportionately many static connections. This suggests that static connections predominate between regions composing the same module, whereas intermodular connections are dynamic. To test this observation in each individual, the proportion of the top-100 most dynamic connections that were intermodular was divided by the overall proportion of *all* intermodular connections. This ratio was significantly greater than unity (ratio: 1.13 ± 0.02 ; $P = 0.0001$; 83 ± 1.5% of top-100 intermodular, 69% of all connections intermodular).

Dynamic connections were significantly more prevalent between spatially distant regions. The mean interregional distance

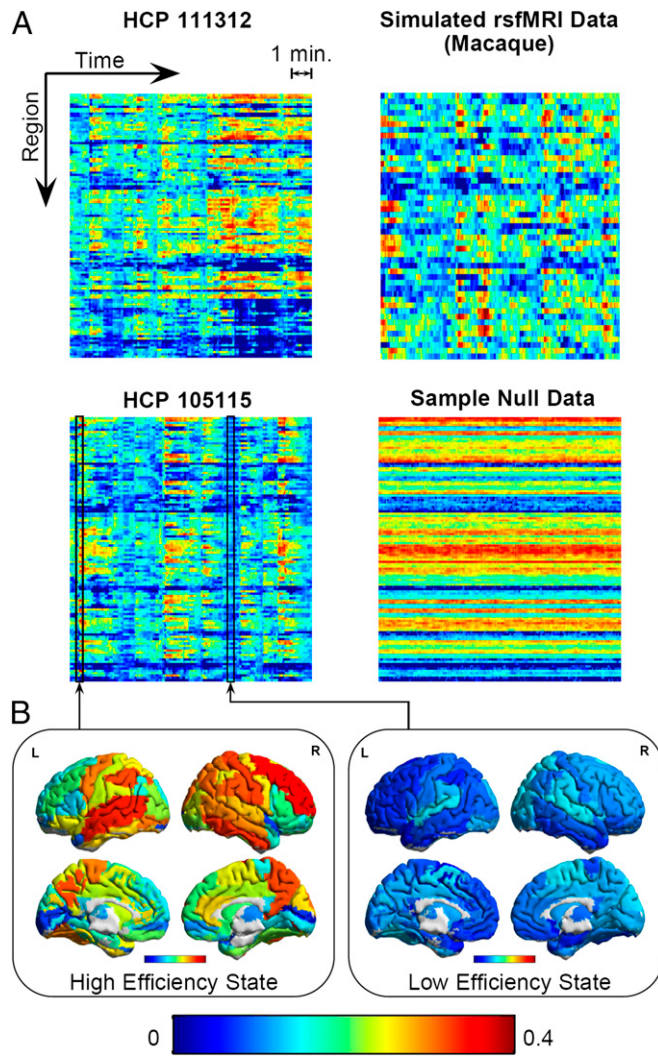


Fig. 3. Time-resolved analysis of regional network efficiency shows that resting-state functional brain networks spontaneously reconfigure in such a way that multiple regions synchronously transition to high-efficiency states. (A) Regional network efficiency for two healthy, young adults; simulated rsfMRI data and a sample null data set. Matrix rows/columns represent regions/time. Efficiency range for simulated data is 0–0.25. (B) Regional efficiencies rendered onto the cortical surface for representative high- and low-efficiency states.

for all connections was 77 mm, whereas the top-100 most dynamic connections were on average 83 ± 1.7 mm ($P = 0.004$). For all individuals, the time-averaged correlation coefficients were significantly anticorrelated with the statistic developed to test for nonstationarity ($r < -0.4$, $P < 0.01$; *SI Appendix*, Fig. S6). Hence, the most dynamic connections were also the connections with the weakest time-averaged correlations. Intermodular connections likely comprised the most dynamic connections because dynamic connections are near zero in the time averages used by the modular decomposition algorithm.

Noise Confounds. Time-resolved analysis of rsfMRI data are particularly susceptible to noise confounds. Confounds include scanner drift, head motion (47), and physiological noise due to variation in respiratory depth/rate (34) and cardiac rate (48). To exclude these confounds as possible causes of the results, for each individual, the principal component explaining the most temporal variation in the top-100 most dynamic connections was regressed against estimates of physiological noise as well as

estimates of instantaneous head motion, namely, displacement and rotation in x , y , and z directions and all associated first-order derivatives. After controlling the false discovery rate at a relatively liberal threshold of 10% across all regressors, no measure of head motion or physiological noise was a significant predictor of connectivity fluctuations for any individual. Noise confounds and principal components are shown in *SI Appendix*, Fig. S7.

Simulated rsfMRI Data. To further exclude noise confounds as a potential explanation for the dynamic behavior that we identified, our findings were replicated using simulated rsfMRI data, which was necessarily free of any head motion, scanner drift, and physiological noise. Neuronal population dynamics were simulated for 47 neural masses interconnected according to the axonal connectivity of the macaque neocortex (31). The Balloon-Windkessel model was then applied to the simulated neuronal dynamics to generate realistic rsfMRI data matched in length and temporal resolution to the HCP data (*SI Appendix*). Using this noise-free, simulated rsfMRI data, we replicated our findings, with regional efficiencies displaying coordinated fluctuations akin to those seen in the HCP data (Fig. 3 and *SI Appendix*, Fig. S8).

Replication Data Set. Our main findings were replicated in an independent data set comprising an unrelated group of 10 individuals (*Material and Methods*). The replication data set was acquired with a different phase encoding and preprocessed using an alternative method for noise removal (30). The null hypothesis of uniformly distributed transitions across time was rejected within all individuals at 0.05 FWER and within 9 of the 10 individuals at 0.01 FWER. Highly synchronized fluctuations in regional efficiency were once again evident in all individuals, as shown for three individuals in *SI Appendix*, Fig. S9.

Discussion

By mapping time-resolved functional brain networks at a sub-second resolution, we here report evidence for dynamic (non-stationary) behavior in the brain's resting state from the scale of simple pairwise temporal correlations to a complex network property. We found that dynamic behavior was coordinated across the cortex, with hemodynamic activity between multiple pairs of spatially distributed regions spontaneously transitioning in and out of correlation over time in a globally coordinated manner.

Our results accord with electroencephalographic and theoretical investigations of dynamic connectivity (1–3) that suggest a “natural partitioning” (1) of functional dynamics into synchronous epochs. Alternating patterns of correlation and anti-correlation may constitute fundamental dynamics of information processing by allowing the formation and dissolution of dynamic cell assemblies (3, 4). Moreover, intermittent epochs of global synchronization may enable otherwise segregated network elements access to a cognitive global workspace, which may be necessary for effortful processing (49). Transient exploration of this workspace may allow the brain to efficiently balance segregated and integrated neural dynamics.

Epochs at which more functional connections transitioned (i.e., crossed their median value) than expected by chance alone were sporadically distributed in time and found in all 10 individuals as well as in a replication data set and simulated rsfMRI data. We hypothesize that these “transition epochs” mark change-over points between distinct metastates (33, 50). Our observation of concomitant changes in a complex network property—network efficiency—suggests that dynamic fluctuations at the pairwise level might be coordinated in such a way as to achieve a topological “objective.”

Our time-resolved analysis of network efficiency revealed that multiple spatially distributed regions simultaneously increased, for brief intervals, their topological efficiency and, by inference, their capacity to transfer information. However, these intervals of high efficiency are supported by long anatomical connections and thus likely carry an extra metabolic cost (44). We argue that

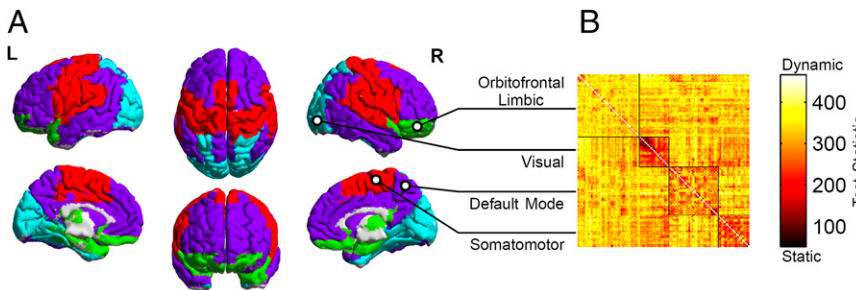


Fig. 4. Dynamic functional connections are more likely to interconnect two distinct modules. (A) Time-averaged decomposition comprising four modules rendered on the cortical surface. (B) Test statistic values averaged over 10 healthy, young adults shown in matrix form. High test statistic values (yellow shades) provide greater evidence for dynamic (nonstationary) fluctuations. Low values indicate static connections. Row/columns are ordered such that regions composing the same module occupy consecutive rows/columns. Modules are delineated with thin black lines.

intermittent periods of high efficiency may hence be a dynamic strategy that has evolved to minimize metabolic requirements, analogous to intermittent search strategies that constitute an optimal solution in settings as diverse as food foraging in animals and eye movements in humans (51). Some of the dynamic regions that we identified have been described as “transmodal” (e.g., default mode parietal areas), owing to their functional associations with multiple intrinsic connectivity networks (ICNs) (52). On the basis that some transmodal regions are also highly dynamic, we suggest that their multiple functional associations may be realized through a dynamic process of time-division multiplexing, where the region is connected with specific ICNs for a fraction of time. A time-averaged analysis may thus reveal the “echoes” (52) of multiple ICNs at transmodal regions.

In this study, we also investigated the role of dynamic behavior with reference to a conventional time-averaged modular decomposition of functional brain networks. We found that the most dynamic connections were intermodular and localized to known hubs of default mode and fronto-parietal systems (36), suggesting that these hubs were connectors linking multiple modules with one another (53). Our results suggest that time-averaged modular decompositions may be explained by differences in the topographic layout of dynamic and static connections. In particular, we found that dynamic connections were typically connections with time-averaged correlations near zero and were thus more likely to straddle two modules. Intramodular connections composing the orbitofrontal-limbic module were relatively dynamic compared with the other three modules identified. This “transitional” module (29) may therefore be more flexible than the others, possibly supporting transient psychological states (19) and complementing frontoparietal regions in supporting adaptive, context-dependent control (28, 54).

Methodological Considerations. First, we used traditional volume-based parcellations of cortical and subcortical regions, as defined by established volumetric atlases. Recent investigations have demonstrated the benefit of surface-based parcellation (30, 55), which may reduce heterogeneity in region size. Larger regions are more likely to encapsulate multiple temporally independent modes (24) that might cancel each other out when averaged. The dynamic behavior in regionally averaged activity may therefore be influenced by region size, although we found no evidence of a linear relation between volume and our index of consistency. Second, we used what is effectively the Pearson (full) correlation coefficient to estimate functional connectivity within each time window. A criticism of full correlation is its sensitivity to indirect functional relations between pairs of regions that are mediated by a third region (38). Third, methodological options for pre-processing rsfMRI data are many and varied. We used pre-processing options recommended by the HCP and replicated our main findings using a different noise removal method applied to an independent data set as well as simulated rsfMRI data that were necessarily free from any noise confounds. We replicated our findings using the “scrubbing” procedure (47) to correct for head motion (*SI Appendix*, Fig. S10), noting that scrubbing should be used cautiously because it introduces variation in the degrees of freedom per time window.

Conclusion. Time-averaged characterizations of functional brain networks are inherently static and as such reduce the rich temporal dynamics of the resting brain to temporal averages. This represents an oversimplification. With an abundance of high temporal resolution rsfMRI data to be released over the next few years, time-resolved analysis of functional brain networks and their topological organization will become a feasible and likely widespread analysis. Here we have shown that dynamic fluctuations in functional connectivity at the pairwise level appear to be coordinated across the brain so as to realize globally coordinated variations in network efficiency over time, which might represent a balance between optimizing information processing and minimizing metabolic expenditure.

Materials and Methods

Functional MRI Data. Minimally preprocessed rsfMRI data for 10 healthy, unrelated adults (age: 22–35, 4 males) were obtained from the Human Connectome Project (13). Data were obtained under the Q2 Data Release and comprised 1,200 frames of multiband, gradient-echo planar imaging acquired during a period of 14 min and 33 s with the following parameters: relaxation time, 720 ms; echo time, 33.1 ms; flip angle, 52°; field of view, 280 × 180 mm; matrix, 140 × 90; and voxel dimensions, 2 mm isotropic. Individuals were fixated on a projected bright crosshair on a dark background during data acquisition. Only one of the four runs acquired for each individual was analyzed in this study (left-right encoded, second session).

Replication Data Set. An independent data set comprising 10 healthy, unrelated adults was obtained under the Q3 Data Release (age: 26–35, 5 males). Right-left encoding runs acquired in the first session were analyzed. Data were already preprocessed using a metaclassification approach applied to independent components (independent component analysis-based X-noisifier) (30). *SI Appendix*, Table S1, provides details of the individuals composing the main and replication data sets.

Time-Resolved Functional Connectivity. Time-resolved functional connectivity was estimated between pairs of regional time series using a tapered sliding-window approach. Tapering provides better suppression of spurious correlations and may reduce sensitivity to outliers. An exponentially tapered window (56) spanning N time points was defined by the weight vector $w_t = w_0 e^{(\tau - N)/\theta}$, $\tau = 1, \dots, N$, $\theta > 0$, and $w_0 = (1 - e^{-1/\theta})/(1 - e^{-N/\theta})$. The weighted Pearson product-moment correlation between region i and region j at time $t \geq N$ was then computed as $\rho_t^{ij} = \sigma_t^{ij}/(\sigma_t^i \sigma_t^j)$, where the weighted SDs, σ_t^i , and the weighted covariances, σ_t^{ij} , are defined in *SI Appendix*. The window length was set to 60 s and the exponent, θ , was set to a third of the window length (56). Statistical analysis was performed on the time-resolved correlation coefficients $\{\rho_t^{ij}\}_{t \geq N}$.

Nonstationarity Test Statistic. A univariate test statistic was developed to measure the extent of time-varying (nonstationary) fluctuations in the time-resolved correlation coefficients for each pair of regions. For a given pair of regions i and j , median crossing points were defined as the set of solutions $\{t_n : \rho_t^{ij} = \mu_t\}_{n=1}^J$, where $\mu_t := \text{median}(\rho_t^{ij})$ and J denotes the total number of median crossing points. A pair of consecutive crossing points (t_n, t_{n+1}) defined an excursion from the median value. The longer and larger the excursions were from the median value, the greater the evidence for nonstationary behavior. A statistic that increased as a function of excursion length and/or height was therefore devised. The length of the n th excursion was the time interval $I_n = t_{n+1} - t_n$. The height of the n th excursion was $h_n = \max\{|\rho_t^{ij} - \mu_t| : t_n < t < t_{n+1}\}$. The final statistic was given by the sum over

all excursions of the length–height product; that is, $T = \sum_{n=1}^{J-1} |h_n^L h_n^B|$, where $0 \leq \alpha, \beta \leq 1$ are parameters controlling the relative weighting between the importance of long versus large excursions. These exponents were empirically set to $\alpha = 0.9$ and $\beta = 1$ in this study, giving a marginally greater weighting to height. Examples of the statistic applied to various stationary and nonstationary time series are provided in *SI Appendix*, Fig. S11.

Vector Autoregressive Null Model. Stable (stationary) VAR models were fitted to the regional time series using maximum-likelihood estimation. VAR model responses were then simulated to generate surrogate regional time series, satisfying the null hypothesis of a linearly correlated, stationary, multivariate stochastic process. This was repeated to generate 250 independent null data sets. The surrogate regional time series comprising each null data set were then processed in the same way as the actual data. This enabled empirical estimation of the null distribution of the test statistic and graph measures evaluated in this study. It was computationally infeasible to fit a single multidimensional VAR model with a covariance structure with dimensions

1. Breakspear M (2004) "Dynamic" connectivity in neural systems: Theoretical and empirical considerations. *Neuroinformatics* 2(2):205–226.
2. Deco G, Jirsa VK, Robinson PA, Breakspear M, Friston K (2008) The dynamic brain: From spiking neurons to neural masses and cortical fields. *PLOS Comput Biol* 4(8):e1000092.
3. Friston KJ (1997) Transients, metastability, and neuronal dynamics. *Neuroimage* 5(2):164–171.
4. Breakspear M, Williams L, Stam K (2004) A novel method for the topographic analysis of phase dynamics in neural systems reveals formation and dissolution of "dynamic cell assemblies." *J Comput Neurosci* 16(1):49–68.
5. Hutchison RM, et al. (2013) Dynamic functional connectivity: Promise, issues, and interpretations. *Neuroimage* 80:360–378.
6. Bullmore E, Sporns O (2009) Complex brain networks: Graph theoretical analysis of structural and functional systems. *Nat Rev Neurosci* 10(3):186–198.
7. Meunier D, Lambiotte R, Bullmore ET (2010) Modular and hierarchically modular organization of brain networks. *Front Neurosci* 4:200.
8. Power JD, Schlaggar BL, Lessov-Schlaggar CN, Petersen SE (2013) Evidence for hubs in human functional brain networks. *Neuron* 79(4):798–813.
9. van den Heuvel MP, Sporns O (2011) Rich-club organization of the human connectome. *J Neurosci* 31(44):15775–15786.
10. van den Heuvel MP, Kahn RS, Goñi J, Sporns O (2012) High-cost, high-capacity backbone for global brain communication. *Proc Natl Acad Sci USA* 109(28):11372–11377.
11. Bassett DS, Bullmore E (2006) Small-world brain networks. *Neuroscientist* 12(6):512–523.
12. Sporns O, Zwi JD (2004) The small world of the cerebral cortex. *Neuroinformatics* 2(2):145–162.
13. Van Essen DC, et al.; WU-Minn HCP Consortium (2013) The WU-Minn Human Connectome Project: An overview. *Neuroimage* 80:62–79.
14. Biswal BB, et al. (2010) Toward discovery science of human brain function. *Proc Natl Acad Sci USA* 107(10):4734–4739.
15. Fox MD, et al. (2005) The human brain is intrinsically organized into dynamic, anti-correlated functional networks. *Proc Natl Acad Sci USA* 102(27):9673–9678.
16. Fox MD, Raichle ME (2007) Spontaneous fluctuations in brain activity observed with functional magnetic resonance imaging. *Nat Rev Neurosci* 8(9):700–711.
17. Greicius MD, Supekar K, Menon V, Dougherty RF (2009) Resting-state functional connectivity reflects structural connectivity in the default mode network. *Cereb Cortex* 19(1):72–78.
18. Sporns O (2012) *Discovering the Human Connectome* (MIT Press, Cambridge, MA).
19. Chang C, Glover GH (2010) Time-frequency dynamics of resting-state brain connectivity measured with fMRI. *Neuroimage* 50(1):81–98.
20. Handwerker DA, Roopchansingh V, Gonzalez-Castillo J, Bandettini PA (2012) Periodic changes in fMRI connectivity. *Neuroimage* 63(3):1712–1719.
21. Hutchison RM, Womelsdorf T, Gati JS, Everling S, Menon RS (2013) Resting-state networks show dynamic functional connectivity in awake humans and anesthetized macaques. *Hum Brain Mapp* 34(9):2154–2177.
22. Keilholz SD, Magnuson ME, Pan WJ, Willis M, Thompson GI (2013) Dynamic properties of functional connectivity in the rodent. *Brain Connect* 3(1):31–40.
23. Kitzbichler MG, Smith ML, Christensen SR, Bullmore E (2009) Broadband criticality of human brain network synchronization. *PLOS Comput Biol* 5(3):e1000314.
24. Smith SM, et al. (2012) Temporally-independent functional modes of spontaneous brain activity. *Proc Natl Acad Sci USA* 109(8):3131–3136.
25. Allen EA, et al. (2014) Tracking whole-brain connectivity dynamics in the resting state. *Cereb Cortex* 24(3):663–676.
26. Jones DT, et al. (2012) Non-stationarity in the "resting brain's" modular architecture. *PLoS ONE* 7(6):e39731.
27. Bassett DS, et al. (2011) Dynamic reconfiguration of human brain networks during learning. *Proc Natl Acad Sci USA* 108(18):7641–7646.
28. Kitzbichler MG, Henson RN, Smith ML, Nathan PJ, Bullmore ET (2011) Cognitive effort drives workspace configuration of human brain functional networks. *J Neurosci* 31(22):8259–8270.
29. Fornito A, Harrison BJ, Zalesky A, Simons JS (2012) Competitive and cooperative dynamics of large-scale brain functional networks supporting recollection. *Proc Natl Acad Sci USA* 109(31):12788–12793.
30. Smith SM, et al.; WU-Minn HCP Consortium (2013) Resting-state fMRI in the Human Connectome Project. *Neuroimage* 80:144–168.
31. Honey CJ, Kotter R, Breakspear M, Sporns O (2007) Network structure of cerebral cortex shapes functional connectivity on multiple time scales. *Proc Natl Acad Sci USA* 104(24):10240–10245.
32. Deco G, Jirsa VK (2012) Ongoing cortical activity at rest: Criticality, multistability, and ghost attractors. *J Neurosci* 32(10):3366–3375.
33. Deco G, Jirsa VK, McIntosh AR (2013) Resting brains never rest: Computational insights into potential cognitive architectures. *Trends Neurosci* 36(5):268–274.
34. Chang C, Glover GH (2009) Relationship between respiration, end-tidal CO₂, and BOLD signals in resting-state fMRI. *Neuroimage* 47(4):1381–1393.
35. Tzourio-Mazoyer N, et al. (2002) Automated anatomical labeling of activations in SPM using a macroscopic anatomical parcellation of the MNI MRI single-subject brain. *Neuroimage* 15(1):273–289.
36. Hagmann P, et al. (2008) Mapping the structural core of human cerebral cortex. *PLoS Biol* 6(7):e159.
37. Raichle ME, et al. (2001) A default mode of brain function. *Proc Natl Acad Sci USA* 98(2):676–682.
38. Zalesky A, Fornito A, Bullmore E (2012) On the use of correlation as a measure of network connectivity. *Neuroimage* 60(4):2096–2106.
39. Beggs JM, Plenz D (2003) Neuronal avalanches in neocortical circuits. *J Neurosci* 23(35):11167–11177.
40. Freyer F, et al. (2011) Biophysical mechanisms of multistability in resting-state cortical rhythms. *J Neurosci* 31(17):6353–6361.
41. Craddock RC, James GA, Holtzheimer PE III, Hu XP, Mayberg HS (2012) A whole brain fMRI atlas generated via spatially constrained spectral clustering. *Hum Brain Mapp* 33(8):1914–1928.
42. Zalesky A, et al. (2010) Whole-brain anatomical networks: Does the choice of nodes matter? *Neuroimage* 50(3):970–983.
43. Achard S, Bullmore E (2007) Efficiency and cost of economical brain functional networks. *PLOS Comput Biol* 3(2):e17.
44. Bullmore E, Sporns O (2012) The economy of brain network organization. *Nat Rev Neurosci* 13(5):336–349.
45. Liang X, Zou Q, He Y, Yang Y (2013) Coupling of functional connectivity and regional cerebral blood flow reveals a physiological basis for network hubs of the human brain. *Proc Natl Acad Sci USA* 110(5):1929–1934.
46. Bassett DS, et al. (2013) Robust detection of dynamic community structure in networks. *Chaos* 23(1):013142.
47. Power JD, et al. (2014) Methods to detect, characterize, and remove motion artifact in resting state fMRI. *Neuroimage* 84:320–341.
48. Chang C, et al. (2013) Association between heart rate variability and fluctuations in resting-state functional connectivity. *Neuroimage* 68:93–104.
49. Dehaene S, Kerszberg M, Changeux JP (1998) A neuronal model of a global workspace in effortful cognitive tasks. *Proc Natl Acad Sci USA* 95(24):14529–14534.
50. Van de Ville D, Britz J, Michel CM (2010) EEG microstate sequences in healthy humans at rest reveal scale-free dynamics. *Proc Natl Acad Sci USA* 107(42):18179–18184.
51. Edwards AM, et al. (2007) Revisiting Lévy flight search patterns of wandering albatrosses, bumblebees and deer. *Nature* 449(7165):1044–1048.
52. Braga RM, Sharp DJ, Leeson C, Wise RJ, Leech R (2013) Echoes of the brain within default mode, association, and heteromodal cortices. *J Neurosci* 33(35):14031–14039.
53. Sporns O, Honey CJ, Kotter R (2007) Identification and classification of hubs in brain networks. *PLoS ONE* 2(10):e1049.
54. Cole MW, et al. (2013) Multi-task connectivity reveals flexible hubs for adaptive task control. *Nat Neurosci* 16(9):1348–1355.
55. Glasser MF, et al.; WU-Minn HCP Consortium (2013) The minimal preprocessing pipelines for the Human Connectome Project. *Neuroimage* 80:105–124.
56. Pozzi F, Di Matteo T, Aste T (2012) Exponential smoothing weighted correlations. *Eur Phys J B* 85(6):1–21.

equal to the number of regions. Two-dimensional VAR models were therefore independently fitted to each pair of regional time series, implying that the model response for a given region was conditional for the pair of regions under consideration. See *SI Appendix* for details of simulation of VAR model responses. This study was approved by the QIMR Human Research Ethics Committee (P1331).

ACKNOWLEDGMENTS. Data were provided by the Human Connectome Project, WU-Minn Consortium (1U54MH091657; Principal Investigators: David Van Essen and Kamil Ugurbil) funded by the 16 National Institutes of Health (NIH) institutes and centers that support the NIH Blueprint for Neuroscience Research; and by the McDonnell Center for Systems Neuroscience at Washington University. We acknowledge support provided by the Australian National Health and Medical Research Council [Career Development Fellowship GNT1047648 (to A.Z.)], Australian Research Council, Monash Larkins Award (to A.F.), Queensland Health Fellowship (to M.B.), and the James S. McDonnell Foundation (M.B. and L.L.G.).

Time-resolved functional brain networks reveal dynamics of human brain connectivity at rest

Supporting Information (SI) Appendix

Andrew Zalesky, Alex Fornito, Luca Cocchi, Leonardo L. Gollo, Michael Breakspear

SI Movies

Cortical renderings of time-resolved regional efficiencies were compiled into AVI format movies for two representative individuals. Parameters: 1440 ms sampling period ($2 \times$ repetition time); 15 frames per second; 1 second in movie time equals 21.6 seconds in real time.

- HCP105115 WMV movie (4 MB)
- HCP111312 WMV movie (4 MB)

Legend for SI Movie HCP105115: Movie of time-resolved regional network efficiencies rendered onto the cortical surface for individual HCP105115.

Legend for SI Movie HCP111312: Movie of time-resolved regional network efficiencies rendered onto the cortical surface for individual HCP111312.

SI Materials and Methods

Functional MRI Preprocessing

Minimally preprocessed rsfMRI data was obtained from the Human Connectome Project (HCP; 1). The minimal preprocessing included was completed according to HCP Functional Pipeline v2.0 (2, 3), which involved: 1) removal of spatial and gradient distortions; 2) correction for head movement; 3) intensity normalization and bias field removal; and, 4) transformation to MNI space (2 mm isotropic) using a single spline re-sampling from the original EPI frames.

Preprocessed EPI frames were bandpass filtered to suppress frequency components outside the range 0.01-0.1 Hz and spatially averaged with respect to established cortical and subcortical regional parcellations to yield representative regional time series (4–6). Regional time series were then subject to standard processing routines to reduce spurious variance unlikely to reflect neuronal activity (7, 8). In particular, the detrended regional time series were regressed against the following nuisance variables: 1) signal averaged from ventricular regions; 2) signal averaged from white matter regions; 3) six detrended head realignment parameters and corresponding derivatives (9); and, 4) physiological noise signals estimated with the CompCor procedure (10). The “broken-stick” method (11) identified between 4 to 6 significant noise components for each individual. All nuisance variables were bandpass filtered before regression (12), but CompCor was applied to the unfiltered data. It is the residuals from these multiple regressions that were

used in subsequent analysis and referred to as the *regional time series* in our work. We use $\{x_i^t\}_{t=1}^T$ to denote the regional time series for the i th region, where T is the total number of time points.

Weighted Pearson Product-Moment Correlation

For a window of length N time points and a weighting vector $\{w_\tau\}_{\tau=1}^N$, the weighted Pearson product-moment correlation (13) between region i and region j at time $t \geq N$ was computed as $\rho_t^{ij} = \sigma_t^{ij}/(\sigma_t^i \sigma_t^j)$, where the weighted means, standard deviations and covariances were given by

$$\begin{aligned}\bar{x}_t^i &= \sum_{\tau=1}^N w_\tau x_{t-N+\tau}^i, & \sigma_t^i &= \sqrt{\sum_{\tau=1}^N w_\tau (x_{t-N+\tau}^i - \bar{x}_t^i)^2}, \\ \sigma_t^{ij} &= \sum_{\tau=1}^N w_\tau (x_{t-N+\tau}^i - \bar{x}_t^i)(x_{t-N+\tau}^j - \bar{x}_t^j).\end{aligned}$$

Null Models for Testing Synchrony in Transition Events

A null model was developed to test whether transition events were uniformly distributed in time. Null data can be generated by randomly redistributing in time all transition events in the actual data. However, this approach does not account for inherent properties of correlation networks that can potentially yield coordinated behavior in the absence of any non-stationary connectivity dynamics. For example, non-stationary fluctuations in the *activity* at a single region may result in coordinated fluctuations in the *connectivity* between that region and many of its neighbors, due to the lack of degrees of freedom when using the correlation coefficient as a measure of connectivity in a network (14). As such, if many connections are found to transition at the same time point, it is possible that these transition events are related to non-stationary fluctuations in the activity at a single region. Transition events that are related in this way should therefore be reduced to a smaller set of unique (i.e. unrelated) transition events.

Related transition events are likely to be topologically clustered around a single node or group of nodes. We therefore defined *related transition events* as any group of connections that: i) transitioned at the same time point; and, ii) formed a connected graph component. For example, transition events occurring at the same time on connections (u, v) and (u, w) were assumed to be related, since both events could have been due to the same behavior at region u . In this example, the connections associated with the two transition events form a connected graph component and are therefore reduced to a single transition event. Identifying related transitions in terms of connected graph components is conservative, since truly unrelated transitions—that is, transitions occurring due to specific dynamic aspects of connectivity (15)—can be neighbors as a matter of chance alone, and thus needlessly reduced to a single transition.

Null data sets were generated by randomly redistributing transition events in time, but preserving any groups of *related* transitions. For example, transition events occurring at the same time on connections (u, v) and (u, w) were related according to the above definition, and thus it was forbidden for (u, v) to be redistributed to time t_i , but (u, w) to t_j , $i \neq j$. A total of 10,000 null data sets were generated as such. For each null data set, the total number of groups of related transition events at each time point was enumerated (i.e. total number of connected components). The greatest of these totals across all time points was then recorded for each null data set to yield the null distribution controlling for the familywise error rate (FWER) across all time points. The null hypothesis of uniformly distributed transition events was rejected if at least one time point was found in the actual data comprising more groups of related transition events than the 99th percentile of the empirical null distribution.

For brevity, we henceforth refer to a *group of related transition events* simply as a *transition event*.

Note that null models based on random correlation networks and randomization at the time series level were not appropriate here because the total number of transition events in the null data cannot be matched to the total number of transitions in the actual rsfMRI data.

Simulation of Vector Autoregressive Null Model

Vector autoregressive (VAR) model responses were simulated to generate surrogate regional time series satisfying the null hypothesis of a linearly correlated, stationary, multivariate stochastic process. This was repeated to generate 250 independent null data sets. The surrogate regional time series comprising each null data set were then processed identically as the actual data. This enabled empirical estimation of the null distribution of the test statistic and graph measures evaluated in this study. It was computationally infeasible to fit a single multidimensional VAR model with a covariance structure with dimensions equal to the number of regions. Two-dimensional VAR models were therefore independently fitted to each pair of regional time series, implying the model response for a given region was conditional on the pair of regions under consideration. The VAR model order was chosen to minimize the Bayesian information criterion (BIC). The BIC was evaluated for model orders between 1 and 50 in unity increments for 500 pairs of regions randomly sampled from the 10 individuals. The BIC was most consistently minimized for a model order of 11, corresponding to a maximum lag of approximately 8 seconds. Model order was not optimized for individual pairs of regions.

VAR model responses were simulated using an approach previously described in the literature (16, 17). In brief, simulations were initialized with a randomly sampled contiguous block of actual time series data. Innovations for the simulated processes were randomly sampled from the innovations (residuals) estimated for the actual data. As such, the innovation term for the simulated process at any given time step comprised a randomly-sampled residual of the VAR fit (16).

Fig. S1 shows the time-averaged cross-correlation, power spectral density, cross power spectral density and amplitude distribution for the actual rsfMRI time series and some sample null data.

To accurately estimate significance thresholds for connection-specific measures, the null distribution samples for each individual connection were pooled to yield a single, highly-resolved null distribution. This assumed the statistical properties among connections were homogeneous under the null hypothesis. Without this pooling, the individual null distributions for each pair of regions would not have comprised a sufficient number of samples to accurately estimate significance thresholds.

Consideration was given to generating null data by phase randomizing (18) the regional time series. However, examples were found where the sliding window derived time series of correlation coefficients remained non-stationary even after the regional time series had been phase randomized. In other words, while phase randomization ensured stationarity of the regional time series, it did not necessarily ensure stationarity of the time series for which the null hypothesis was tested; namely, the time-resolved correlation coefficients.

Graph Analysis

To compute efficiency for a given region, shortest path lengths were determined between that region and all other regions in the network. That region's efficiency was then given by the sum of the reciprocal of these shortest path lengths, normalized by one less the total number of regions comprising the network (19). Shortest path lengths were calculated for networks with a fixed connection density of 20%. Specifically, the top 20% largest connections according to correlation coefficient were identified and left untouched, while all other connections were set to zero. This calculation was repeated for each time-resolved connectivity matrix to yield a time series of regional efficiencies. Using a fixed connection density ensured efficiency fluctuations in time were not due to variability in this confound. The weight of a connection for shortest path calculation was taken as the reciprocal of its time-resolved correlation coefficient.

Newman's spectral algorithm (20) was used to decompose the time-averaged connectivity matrices for each individual into modules. Modules defined non-overlapping groups of regions for which the connectivity between regions within the same module was stronger than the connectivity between regions residing in different modules. Two passes of the consensus algorithm (21) were used to determine a modular decomposition representing consensus among the 10 individuals. The first pass was performed separately for each individual and was used to find a stable partition among 100 independent decompositions. The second pass was used to find consensus among the 10 co-occurrence matrices generated by the first pass, yielding a single “median” decomposition that was most similar, on average, to the decomposition for each individual. Cortical renderings were visualized with BrainNet Viewer (22).

Simulated rsfMRI Data

Neuronal population dynamics were simulated for 47 neural masses representing visual, somatosensory and motor cortical regions comprising the macaque neocortex (23). Neural masses were interconnected according to an established binary connectivity matrix originally derived from the CoCoMac database (24). This connectivity matrix is available as part of the Brain Connectivity Toolbox (BCT; 25) and has been previously used to interconnect networks of neural masses (26). While anatomical connectivity matrices can be mapped for the whole human brain using diffusion imaging and tractography, these matrices are undirected and therefore do not preserve key network motifs (27). In contrast, axonal connectivity mapped in the CoCoMac database is directed.

We broadly followed the approach used by (28) to simulate rsfMRI data. In brief, each neural mass was modeled with a set of three coupled differential equations derived from the model of Morris and Lecar, but with several important adaptations (29). Neural masses were coupled according to the axonal connectivity matrix of the macaque neocortex described above. Axonal conduction delays were not modeled between coupled neural masses. The excitatory coupling coefficient was set to 0.04. The weight of each non-zero connection was randomly sampled from a Gaussian distribution with mean of 0.5 and a standard deviation of 0.1 (28).

The full system of coupled differential equations was simulated for a period of 16 minutes with a first-order method at a fixed resolution of 0.2 ms. The first 2 minutes were subsequently discarded to account for possible transient effects persisting from the initial conditions.

The Balloon-Windkessel hemodynamic model (30) was then applied to generate rsfMRI data matched in length and temporal resolution to the HCP data. The neuronal input to the hemodynamic model was the absolute value of the time derivative of the simulated mean excitatory membrane potential, which has been considered a proxy for glutamate turnover (28). The hemodynamic model was simulated independently for each neural mass using a Runge-Kutta method with a fixed step length of 1 ms. The hemodynamic response was then downsampled to a temporal resolution of 720 ms to match the HCP data.

After downsampling, the simulated rsfMRI data was analysed identically to the HCP rsfMRI data. Importantly, the simulated data was necessarily free of any head motion, scanner drift and physiological noise. Hence, replicating our findings in the simulated rsfMRI data excluded these noise confounds as a potential explanation of our results.

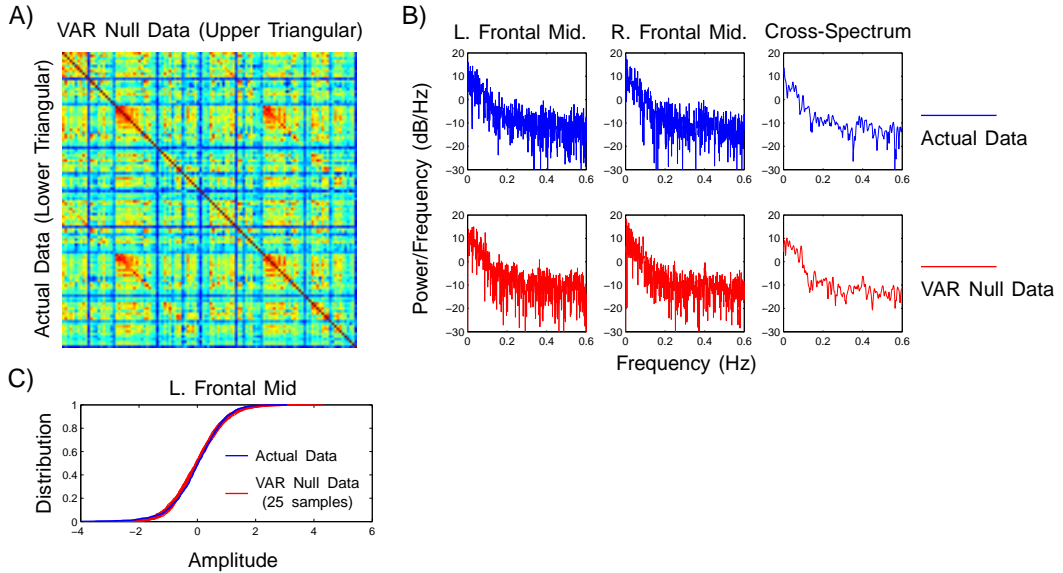


Fig. S1 : The VAR null model generated surrogate time series that were well matched to the time-averaged cross-correlation, power spectral density, cross power spectral density and amplitude distribution of the actual rsfMRI time series. *A)* Time-averaged correlation matrix computed using rsfMRI data (lower triangular) and a sample VAR null data set (upper triangular). *B)* Power spectrum for two representative regions (left and right middle frontal gyrus) and their cross-spectrum computed using the actual rsfMRI data (blue lines) and a sample null data set (red lines). *C)* Regional time series amplitude distribution for the left middle frontal gyrus and 25 null data sets. Data for HCP105115.

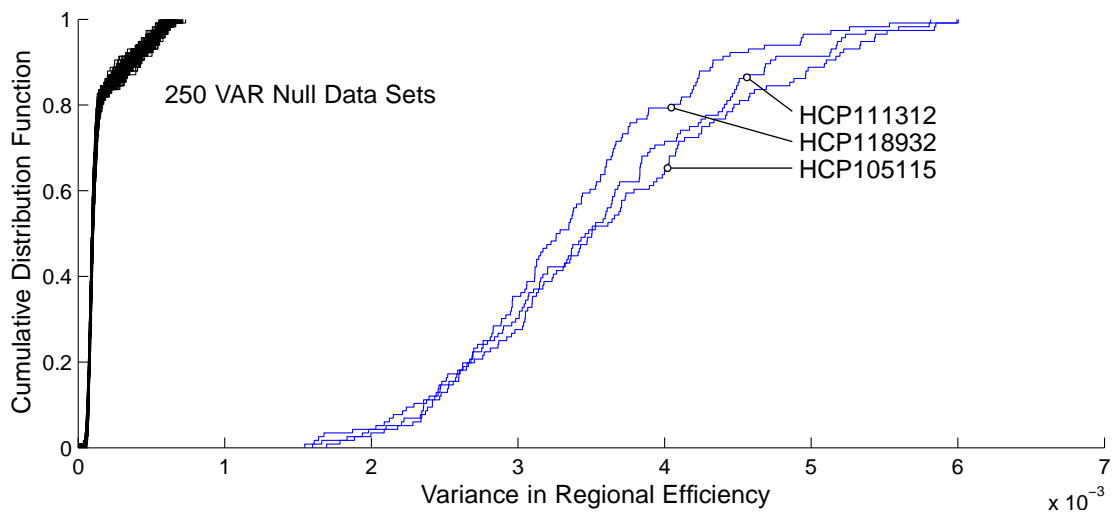


Fig. S2 : The variance in regional efficiency over time was computed for each region in the actual data and in 250 VAR null data sets. The cumulative distribution function of the variance in efficiency is shown for three healthy, young adults (blue lines) and 250 null data sets (black lines).

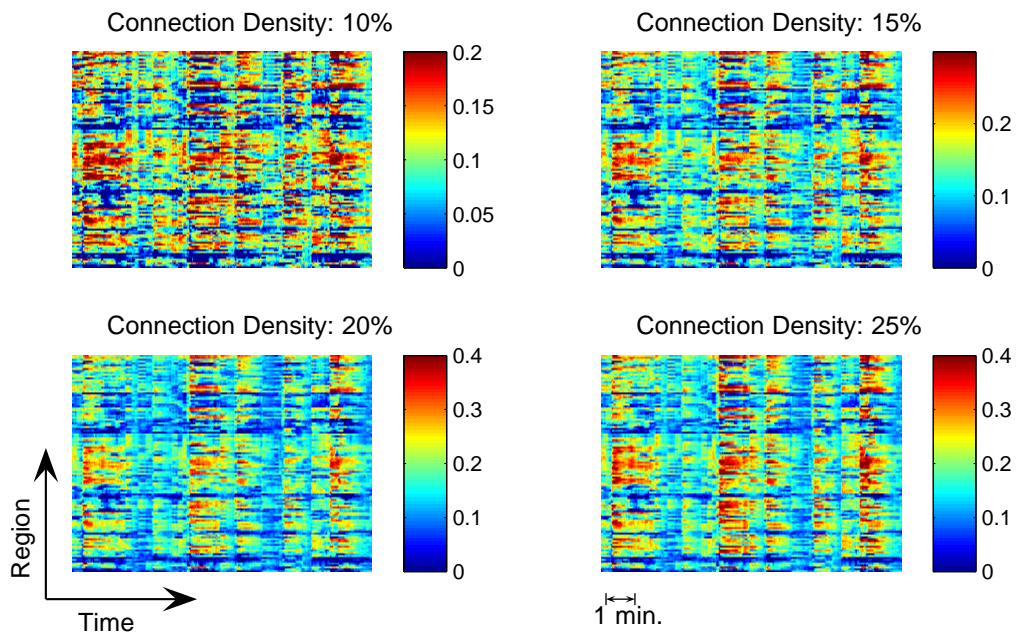


Fig. S3 : Time-resolved regional efficiencies computed using different network connection densities for a healthy, young adult (HCP105115). Note that the color scale varies across connection densities to accommodate global efficiency increases with increasing connection density.

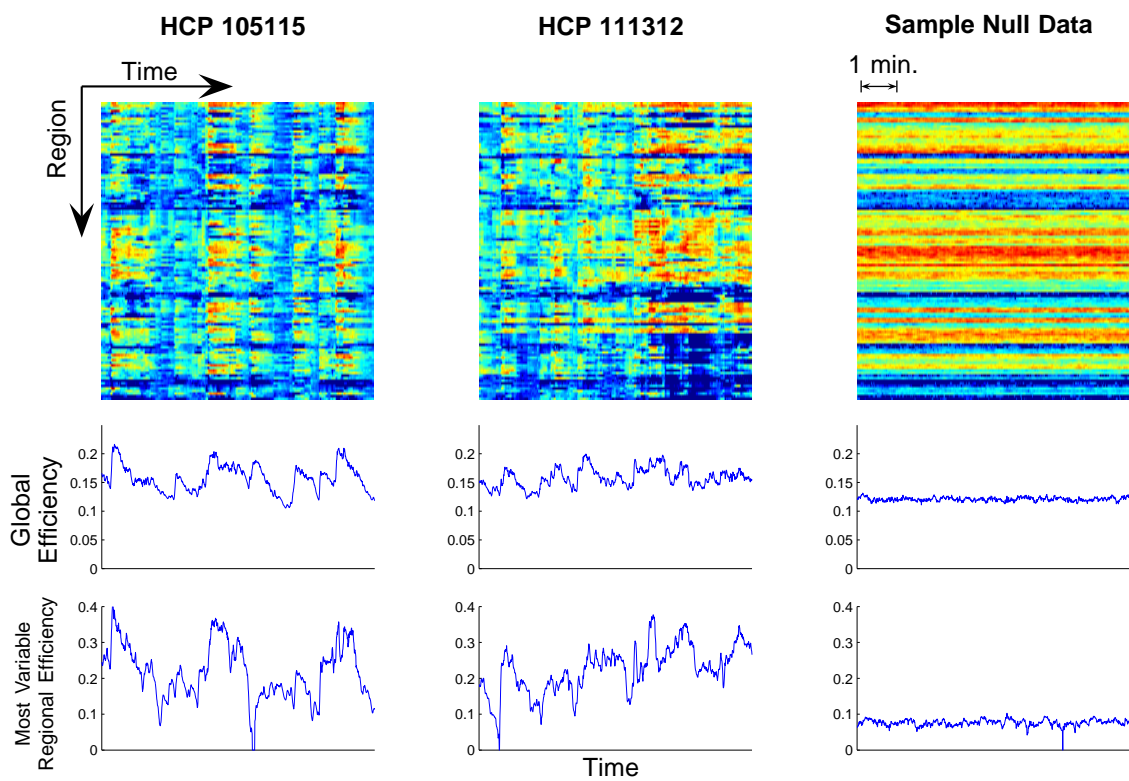


Fig. S4 : *Upper:* Time-resolved regional efficiencies for two healthy, young adults and a sample null data set. *Middle Axes:* Regional efficiencies averaged across all regions to yield a measure of time-resolved global efficiency. *Lower Axes:* Time series of regional efficiency values for the region with the greatest variation in regional efficiency.

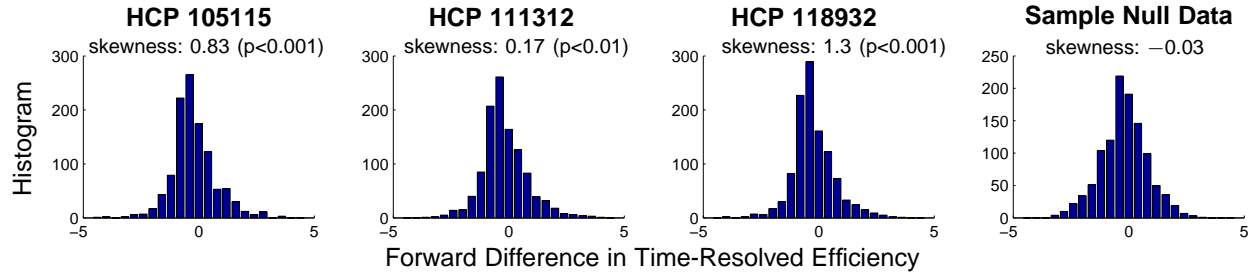


Fig. S5 : The skewness in the forward difference of time-resolved global efficiency was computed in the actual data and in 250 VAR null data sets. Forward differences were significantly positively skewed for all individuals ($p < 0.01$; skewness range: 0.17-1.3). Histograms of forward differences are shown for three healthy, young adults and a sample null data set. The p -value for each individual was given by the proportion of null data sets with skewness of greater or equal value than the observed skewness. Positive skewness is consistent with the observation that transitions from low-to-high efficiencies are sudden, whereas high-to-low transitions are gradual.

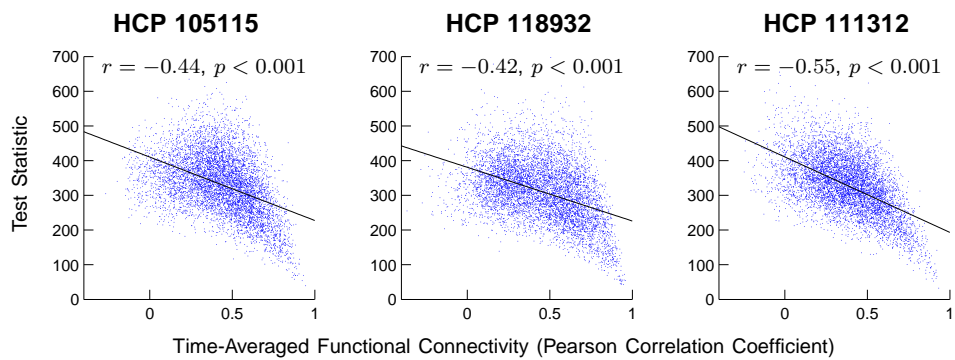
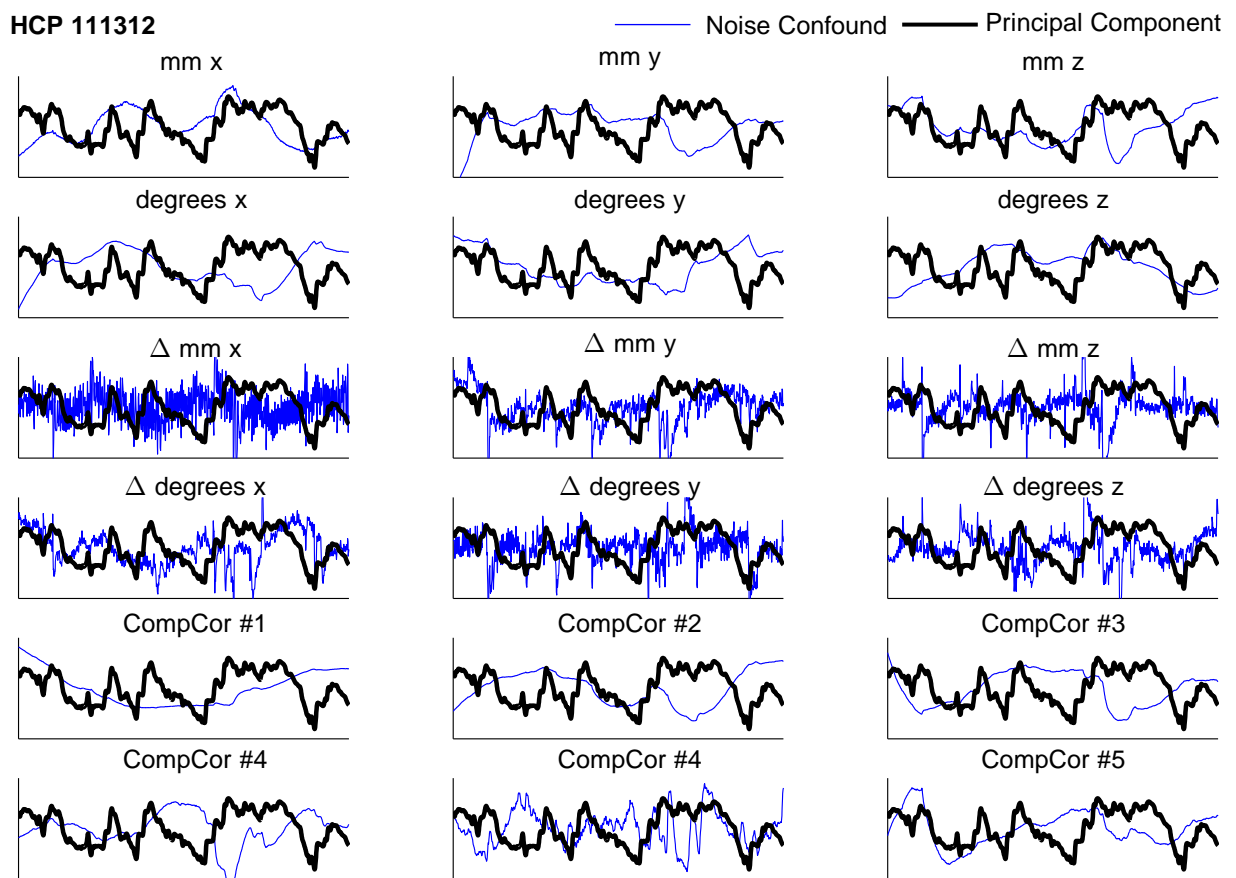
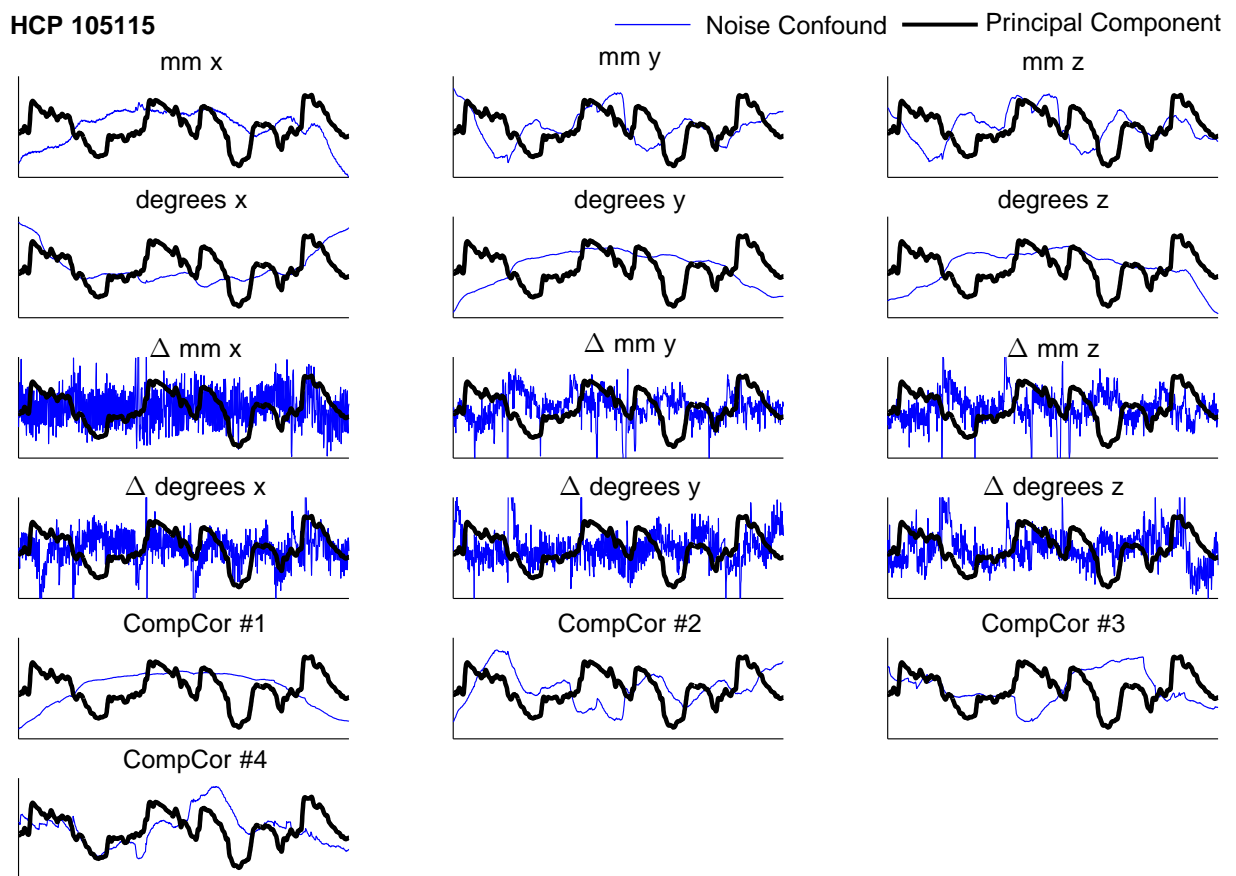


Fig. S6 : Time-averaged correlation coefficients were significantly correlated with the statistic developed to test for time-varying connectivity. Scatter plots characterizing this relation are shown for three healthy, young adults. Lines of best fit are also shown. Each data point (blue dot) represents a connection.



(A) HCP 111312



(B) HCP 105115

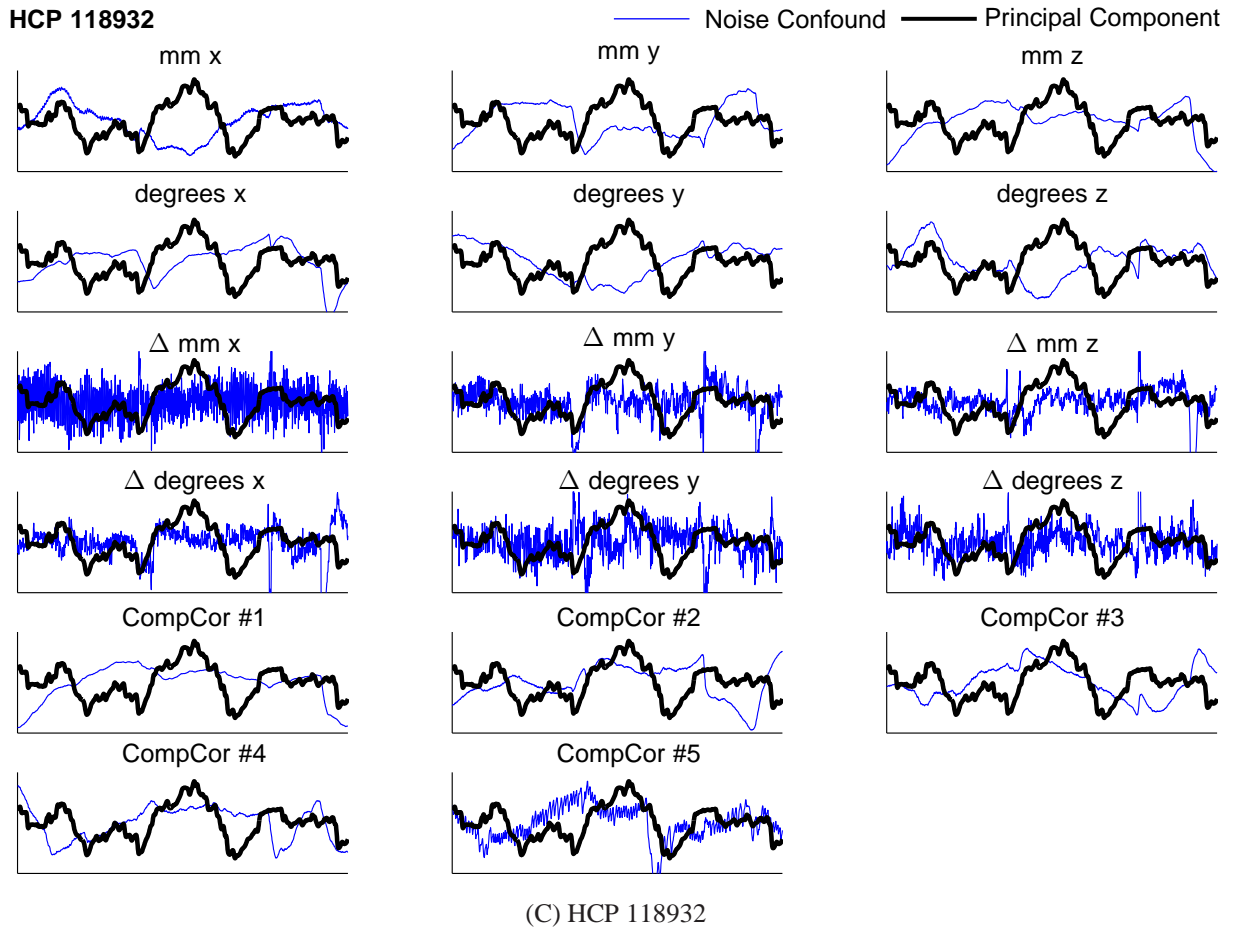


Fig. S7 : The principal component (thick black line) explaining the most temporal variation in the top-100 most dynamic connections was regressed against estimates of physiological noise derived using CompCor (10) as well as estimates of instantaneous head motion; namely, displacement and rotation in x , y and z directions and all associated first-order derivatives, denoted with Δ . Each of these noise confounds was first smoothed with the exponential weight vector used for the sliding window analysis (see *Materials and Methods*). This ensured the smoothing extent and degrees-of-freedom of the noise confounds was matched to the principal component. None of the noise confounds (blue lines) were significant predictors of the principal component for any individual. Note that two principal components explaining at least 20% of the variation for HCP 118932 were found, but only one is shown.

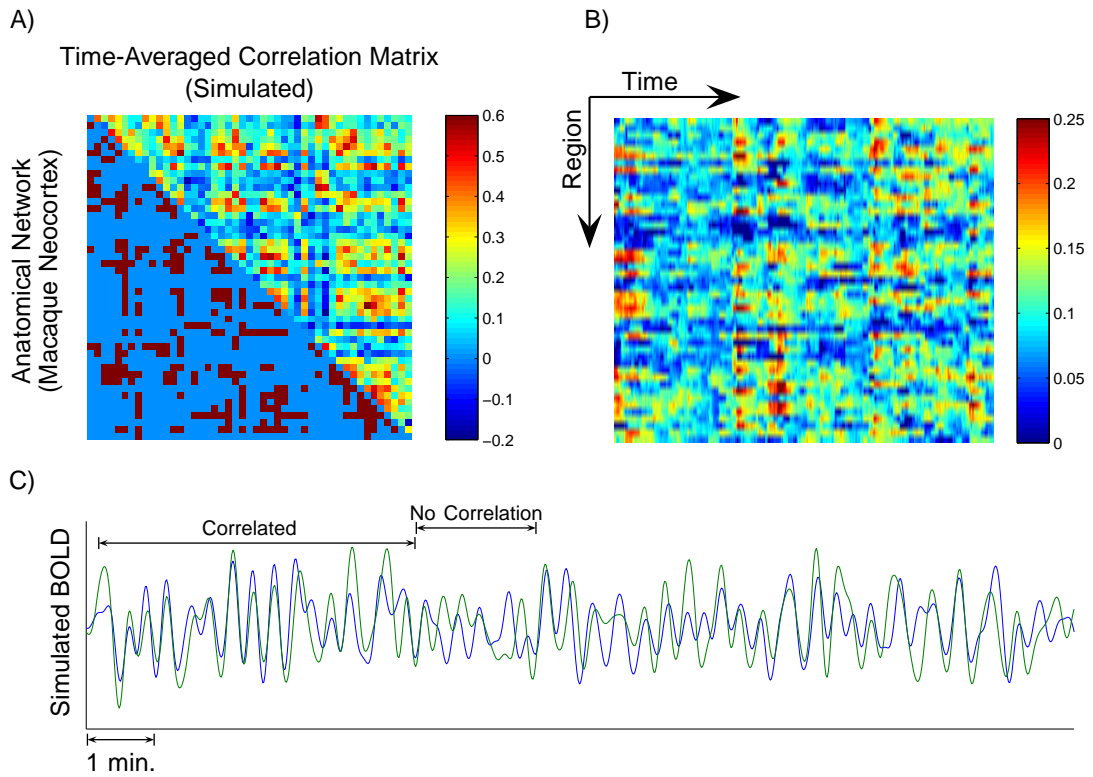


Fig. S8 : Replication of main results with simulated rsfMRI data. The Balloon-Windkessel hemodynamic model was applied to neuronal population dynamics generated by 47 neural masses interconnected according to the anatomical connectivity of the macaque neocortex. **A)** Anatomical connectivity matrix for the macaque neocortex (lower triangular; dark cells indicate a connection) and the time-averaged correlation matrix computed using simulated rsfMRI data (upper triangular). **B)** Time-resolved regional network efficiencies. Matrix row/columns represent regions/time. **C)** Simulated BOLD dynamics for a pair of strongly correlated regions (i.e. neural masses). Despite strong time-averaged correlation (Pearson correlation: 0.54), transient intervals with no correlation are evident.

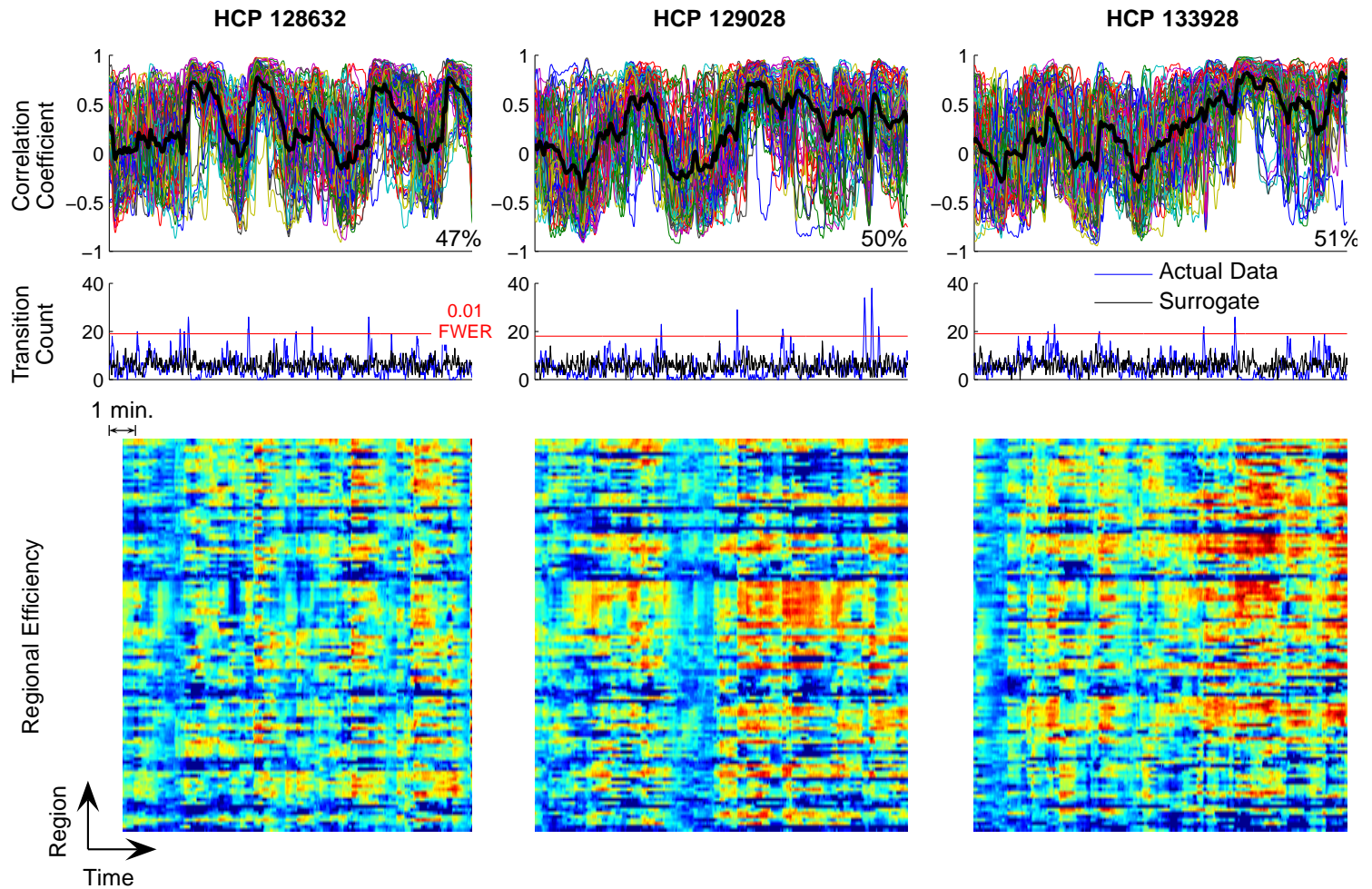


Fig. S9 : Replication of main results with an independent data set. *Upper Axes*: Time series of correlation coefficients pertaining to the top-100 most dynamic functional connections for three healthy, young adults comprising the replication data set. Percentages indicate the amount of variance explained by the principal component (thick black lines). *Middle Axes*: The transition count (blue lines) enumerates for each time point the number of connections that cross their median correlation value. The transition count for a sample null data set is also shown (black lines). The null hypothesis of uniformly distributed transitions across time was rejected at time points when the 0.01 FWER cutoff value (horizontal red lines) was exceeded. *Lower*: Time-resolved regional network efficiencies for the same three individuals. Matrix rows/columns represent regions/time.

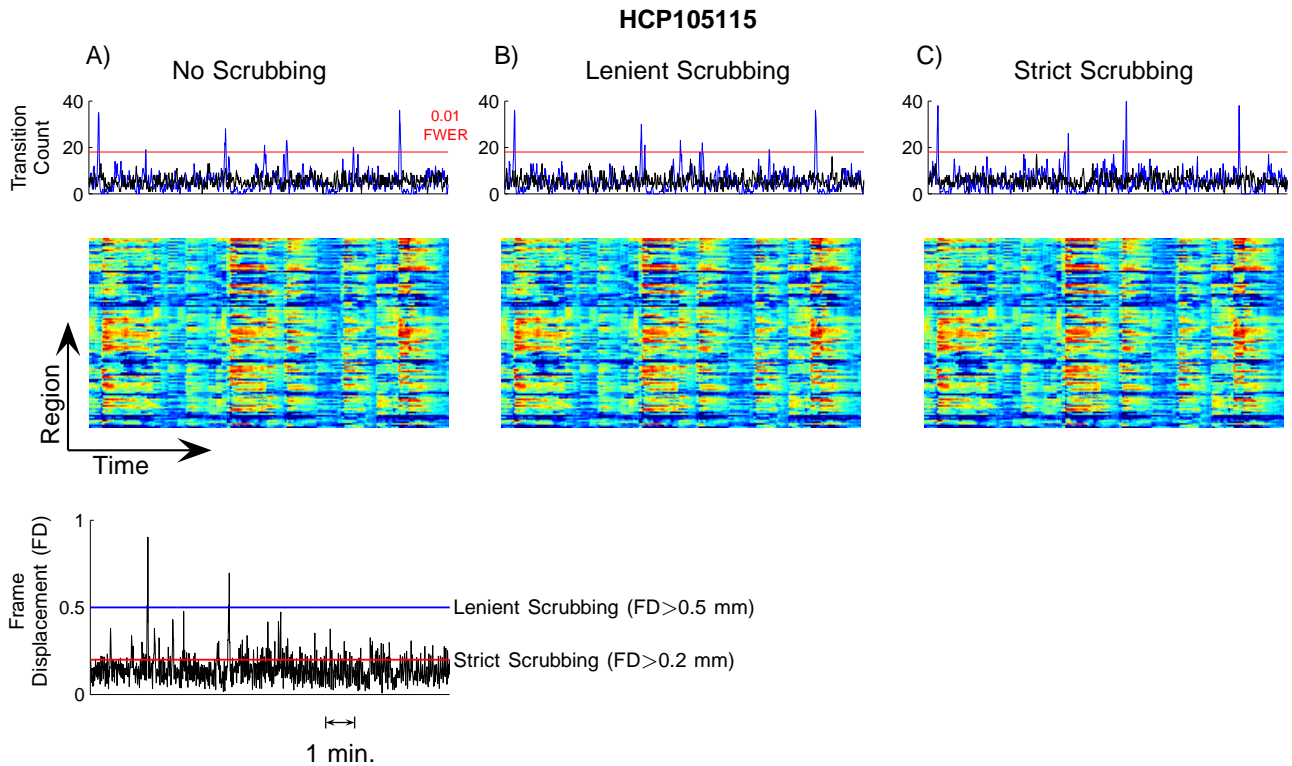


Fig. S10 : Replication of main results for a healthy, young adult (HCP105115) with scrubbing performed to alleviate head motion, in addition to the standard preprocessing steps used to control for noise confounds (31–33). Instantaneous head motion was indexed with a scalar quantity known as frame displacement (FD; 31). *A*) No scrubbing. *B*) Lenient scrubbing ($FD > 0.5 \text{ mm}$). *C*) Stringent scrubbing ($FD > 0.2 \text{ mm}$). *Upper Axes*: The transition count (blue lines) enumerates for each time point the number of connections that cross their median correlation value. The transition count for a sample null data set is also shown (black lines). The null hypothesis of uniformly distributed transitions across time was rejected at time points when the 0.01 FWER cutoff value (horizontal red lines) was exceeded. The null hypotheses was rejected with and without scrubbing *Middle*: Time-resolved regional network efficiencies for the same three individuals. Matrix rows/columns represent regions/time. *Lower Axes*: Frame displacement (FD) as a function of time, with lenient and stringent scrubbing thresholds indicated.

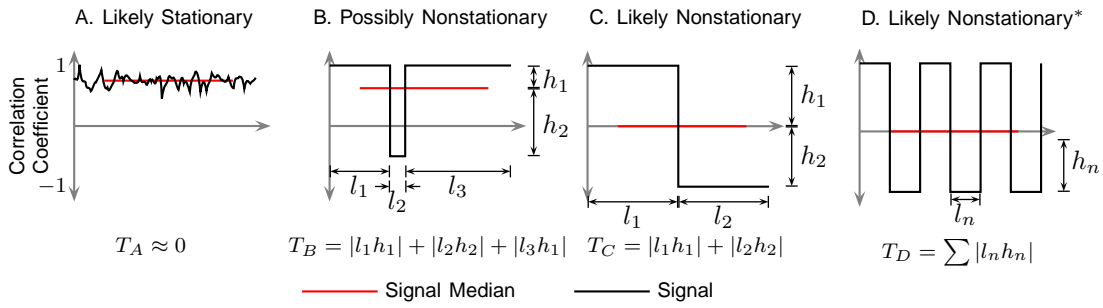


Fig. S11 : Test statistic exemplified for various stationary and non-stationary time series. Non-stationarity is quantified empirically by the existence of *long* and *large* excursions from the median value (red line). Consecutive crossing points of the median define a single excursion. The time between consecutive crossing points defines an excursion's length, l_n . The height, h_n , of an excursion is the maximum separation reached between the time series and its median value. The test statistic is given by the sum over all excursions of the length-height product; that is, $T = \sum |l_n h_n|$. Evidence against the null of a stationary time series increases in the four examples given from left to right; namely, $T_A < T_B < T_C = T_D$. *It can be argued that the center-right time series (C) shows greater evidence of non-stationarity than the rightmost time series (D) because it comprises excursions that are twice as long. To account for this, the statistic can be normalized by the total number of excursions. Under this normalization, $T_C^* > T_D^*$.

Table S1 : Basic demographics and preprocessing method for main and replication data sets.

Main Data Set				Replication Data Set			
Subject Identifier	Sex	Age	Preprocessing	Subject Identifier	Sex	Age	Preprocessing
100307	F	26-30	CompCor	123117	M	26-30	ICA+Fix
103414	F	22-25	CompCor	124422	F	31-35	ICA+Fix
105115	M	31-35	CompCor	125525	F	31-35	ICA+Fix
110411	M	31-35	CompCor	128632	F	31-35	ICA+Fix
111312	F	31-35	CompCor	129028	M	26-30	ICA+Fix
113619	F	31-35	CompCor	130013	M	26-30	ICA+Fix
115320	F	31-35	CompCor	133928	M	26-30	ICA+Fix
117122	F	31-35	CompCor	135932	F	26-30	ICA+Fix
118730	M	22-25	CompCor	136833	M	31-35	ICA+Fix
118932	M	26-30	CompCor	139637	F	31-35	ICA+Fix

References

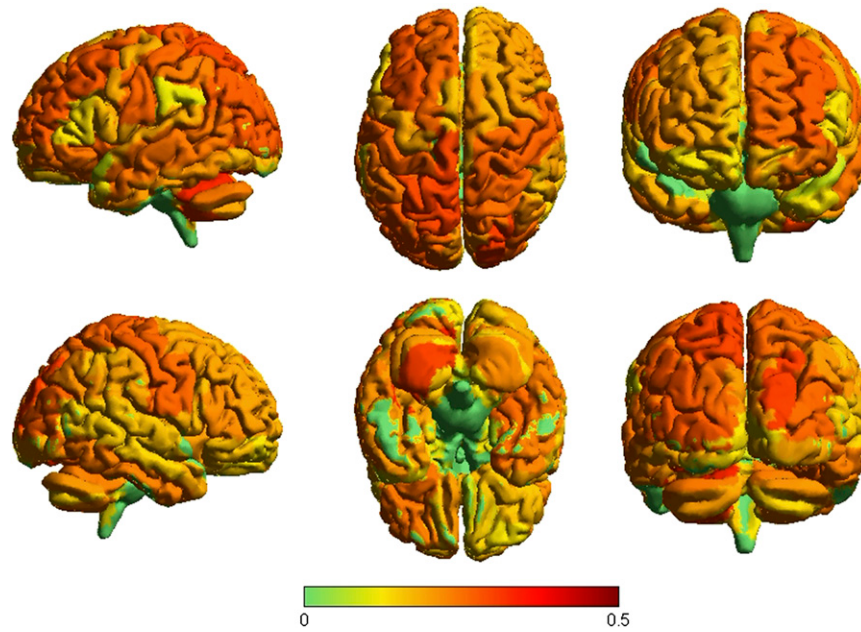
- [1] van Essen DC, Smith SM, Barch DM, Behrens TEJ, Yacoub E, Ugurbil K, WU-Minn HCP Consortium (2013) The WU-Minn Human Connectome Project: An overview. *Neuroimage*. 80:62-79.
- [2] Glasser MF, Sotiropoulos SN, Wilson JA, Coalson TS, Fischl B, Andersson JL, Xu J, Jbabdi S, Webster M, Polimeni JR, Van Essen DC, Jenkinson M; WU-Minn HCP Consortium (2013) The minimal preprocessing pipelines for the Human Connectome Project. *Neuroimage*. 80:105-24.
- [3] Smith SM, Beckmann CF, Andersson J, Auerbach EJ, Bijsterbosch J, Douaud G, Duff E, Feinberg DA, Griffanti L, Harms MP, Kelly M, Laumann T, Miller KL, Moeller S, Petersen S, Power J, Salimi-Khorshidi G, Snyder AZ, Vu AT, Woolrich MW, Xu J, Yacoub E, Ugurbil K, Van Essen DC, Glasser MF; WU-Minn HCP Consortium (2013) Resting-state fMRI in the Human Connectome Project. *Neuroimage*. 80:144-68.
- [4] Fornito A, Zalesky A, Bullmore ET (2010) Network scaling effects in graph analytic studies of human resting-state FMRI data. *Front Syst Neurosci*. 17(4):22.
- [5] Stanley ML, Moussa MN, Paolini BM, Lyday RG, Burdette JH, Laurienti PJ (2013) Defining nodes in complex brain networks. *Front Comput Neurosci*. 22(7):169.
- [6] Zalesky A, Fornito A, Harding IH, Cocchi L, Yucel M, Pantelis C, Bullmore ET (2010) Whole-brain anatomical networks: does the choice of nodes matter? *Neuroimage*. 50(3):970-83.
- [7] Fox MD, Zhang D, Snyder AZ, Raichle ME (2009) The global signal and observed anticorrelated resting state brain networks. *J. Neurophysiol*. 101:3270-83.
- [8] Murphy K, Birn RM, Bandettini PA (2013) Resting-state fMRI confounds and cleanup. *Neuroimage*. 80:349-59.
- [9] Satterthwaite TD, Wolf DH, Loughead J, Ruparel K, Elliott MA, Hakonarson H, Gur RC, Gur RE (2012) Impact of in-scanner head motion on multiple

- measures of functional connectivity: relevance for studies of neurodevelopment in youth. *Neuroimage*. 60(1):623-32.
- [10] Behzadi Y, Restom K, Liau J, Liu TT (2007) A component based noise correction method (CompCor) for BOLD and perfusion based fMRI. *Neuroimage*. 37(1):90-101.
 - [11] Jackson DA (1993) Stopping rules in principal components analysis: a comparison of heuristical and statistical approaches. *Ecology*. 74(8):2204-214.
 - [12] Hallquist MN, Hwang K, Luna B (2013) The nuisance of nuisance regression: spectral misspecification in a common approach to resting-state fMRI preprocessing reintroduces noise and obscures functional connectivity. *Neuroimage*. 82:208-25.
 - [13] Pozzi F, Di Matteo T, Aste T (2012) Exponential smoothing weighted correlations. *The European Physical Journal B*, 85(6):1-21.
 - [14] Zalesky A, Fornito A, Bullmore E (2012) On the use of correlation as a measure of network connectivity. *Neuroimage*. 60(4):2096-106.
 - [15] Breakspear M (2004) “Dynamic connectivity”: Theoretical and empirical considerations. *Neuroinformatics*. 2:205-26.
 - [16] Chang C, Glover GH (2010) Time-frequency dynamics of resting-state brain connectivity measured with fMRI. *Neuroimage*. 50(1):81-98.
 - [17] Stine RA (1987) Estimating properties of autoregressive forecasts. *J Am Stat Assoc*. 82:1072-1078.
 - [18] Theiler J, Eubank S, Longtin A, Galdrikan B, Farmer JD (1992) Testing for nonlinearity in time series: The method of surrogate data. *Physica D* 58:77-94.
 - [19] Achard S, Bullmore E (2007) Efficiency and cost of economical brain functional networks. *PLoS Comput Biol*. 3(2):e17.
 - [20] Newman ME (2006) Modularity and community structure in networks. *Proc Natl Acad Sci U S A*. 103(23):8577-82.
 - [21] Lancichinetti A, Fortunato S (2012) Consensus clustering in complex networks. *Sci Rep*. 2:336.
 - [22] Xia M, Wang J, He Y (2013) BrainNet Viewer: A Network Visualization Tool for Human Brain Connectomics. *PLoS ONE* 8(7):e68910.
 - [23] Felleman DJ, Van Essen DC (1991) Distributed hierarchical processing in the primate cerebral cortex. *Cereb Cortex*. 1:1-47.

- [24] Kötter R (2004) Online retrieval, processing, and visualization of primate connectivity data from the CoCoMac database. Neuroinformatics. 2:127-144.
- [25] Rubinov M, Sporns O (2010) Complex network measures of brain connectivity: uses and interpretation. Neuroimage 52(3):1059-69.
- [26] Honey CJ, Kötter R, Breakspear M, Sporns O (2007) Network structure of cerebral cortex shapes functional connectivity on multiple time scales. Proc Natl Acad Sci U S A. 104(24): 10240-5.
- [27] Gollo LL , Mirasso C, Sporns O, Breakspear M (2014) Mechanisms of zero-lag synchronization in cortical motifs. *PLoS Comput Biol.* 10(4):e1003548.
- [28] Honey CJ, Sporns O, Cammoun L, Gigandet X, Thiran JP, Meuli R, Hagmann P (2009) Predicting human resting-state functional connectivity from structural connectivity. Proc Natl Acad Sci U S A. 106(6):2035-40.
- [29] Breakspear M1, Terry JR, Friston KJ (2003) Modulation of excitatory synaptic coupling facilitates synchronization and complex dynamics in a biophysical model of neuronal dynamics. Network. 14(4):703-32.
- [30] Friston KJ, Harrison L, Penny W (2003) Dynamic causal modelling. Neuroimage. 19(4):1273-302.
- [31] Power JD, Barnes KA, Snyde AZ, Schlaggar BL, Petersen SE (2012) Spurious but systematic correlations in functional connectivity MRI networks arise from subject motion. Neuroimage. 59(3):2142-54.
- [32] Power JD, Mitra A, Laumann TO, Snyder AZ, Schlaggar BL, Petersen SE (2014) Methods to detect, characterize, and remove motion artifact in resting state fMRI. Neuroimage. 84:320-41.
- [33] Yan CG, Cheung B, Kelly C, Colcombe S, Craddock RC, Di Martino A, Li Q, Zuo XN, Castellanos FX, Milham MP (2013) A comprehensive assessment of regional variation in the impact of head micromovements on functional connectomics. Neuroimage. 76:183-201.

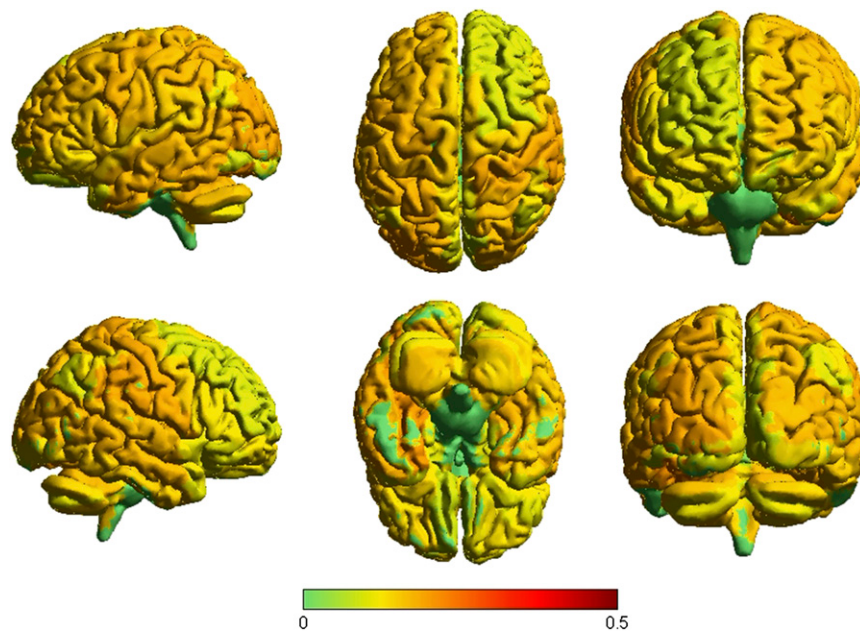
Supporting Information

Zalesky et al. 10.1073/pnas.1400181111



Movie S1. Movie of time-resolved regional network efficiencies rendered on the cortical surface for individual HCP105115. Cortical renderings of time-resolved regional efficiencies were compiled into AVI format movies for two representative individuals. Parameters: 1,440-ms sampling period (2 × repetition time); 15 frames per second; 1 s in movie time equals 21.6 s in real time.

[Movie S1](#)



Movie S2. Movie of time-resolved regional network efficiencies rendered on the cortical surface for individual HCP111312. Cortical renderings of time-resolved regional efficiencies were compiled into AVI format movies for two representative individuals. Parameters: 1,440-ms sampling period (2 × repetition time); 15 frames per second; 1 s in movie time equals 21.6 s in real time.

[Movie S2](#)

Other Supporting Information Files

[SI Appendix \(PDF\)](#)